Cold multinucleon transfer and formation of a dinuclear complex

M. Wilpert, B. Gebauer, Th. Wilpert, W. von Oertzen,* H.G. Bohlen, and J. Speer†
Hahn-Meitner-Institut Berlin, Glienicker Strasse 100, D-14109 Berlin, Germany
(Received 8 March 1994)

Using a kinematical coincidence setup with ΔE-E identification two-body reactions between medium heavy nuclei were studied in the vicinity of the Coulomb barrier. The measured angular distributions for transfer of up to four protons with additional transfer of neutrons show maxima at large c.m. angles of 120–140°. For one- and partially for two-proton transfers the angular distributions are consistent with a one-step transfer mechanism, described by a distorted-wave Born approximation (DWBA) approach. The angular distributions of the three- and four-proton transfers show components in the forward angular region which cannot be described by DWBA. These contributions are interpreted as originating from the decay of a dinuclear complex; for this complex a lifetime of $\tau=6^{+6}_{-2}\times10^{-22}$ s is deduced from the angle of rotation.

PACS number(s): 25.70.Bc, 25.70.Hi

I. INTRODUCTION

In the study of interactions of nuclei, a variety of phenomena is observed, which are connected with the formation of a dinuclear complex. Deeply inelastic collisions have been studied extensively over a wide range of energies and masses [1–3]. The characteristic properties can be characterized by two facts.

(1) Fast energy dissipation predominantly via nucleon exchange; the energy sharing and population of final states in the two final fragments is almost completely determined by statistical equilibrium.

(2) The shape degrees of freedom are also in equilibrium, subject to the macroscopic forces determined by liquid-drop energy and centrifugal energy. The evolution of the dinuclear complex and its lifetime (rotation) depends on the balance of these macroscopic forces.

In the other extreme of quasielastic reactions the population of states and the possible mass fragmentation in the final channel are completely determined by spectroscopic properties of the participating nuclei. In many cases also the multinucleon transfer can be described by a sequence of reaction steps, which are all well described by a first order perturbation theory [4–7]. In more recent works on reactions at and below the Coulomb barrier, a close connection between reaction channels (few-nucleon transfer and inelastic excitation) and the fusion process has been established. Generally, a strong coupling situation between various channels is established [8–10]. The path to fusion can finally be viewed as passing through a moderately excited dinuclear system, just as in the case of deeply inelastic collisions [10].

The present work was aimed at the study of multinucleon-transfer reactions for energies at or below the barrier in order to establish the properties of the cold dinuclear complex that can be formed in these cases. For such a study the variation of the energy in small steps close to and above the barrier is very important, in order to establish the properties of a cold multinucleon transfer or of a more damped reaction. In these studies we were guided by the fact that for cold and moderately excited nuclei, strong shell corrections are predicted in the mass region of $A \approx 140$–150 for particular shapes (quadrupole moments) and mass asymmetries (octupole-moments) [11,12]. Eventually, a connection to predicted superdeformed and hyperdeformed shapes in nuclei can be considered, because the short-lived dinuclear complex may actually fission, showing features similar to those observed in cold fission [13], or a strongly deformed compound nucleus may be formed, which will show strongly collective γ transitions.

For the present study, systems have been chosen with a total mass of the composite nucleus of $A \approx 140$–150. Here the saddle point for two-body decay corresponds to a shape with a pronounced thin neck. The nuclei (isotopes) of target and projectile were further adequately chosen as to assure optimum conditions for multiproton transfer; by this choice a large change of the mass asymmetry in a quasielastic reaction process becomes possible, and the formation of a cold dinuclear complex has a large probability.

Part of the results have already been published [14]. In the present paper in Sec. II we give more details on the experimental setup. In Sec. III the experimental results are given and an analysis in terms of a first order multistep transfer process is discussed in Sec. IV. In Sec. V an interpretation of the results on multinucleon transfer in terms of the formation of a dinuclear complex is attempted. A comparison with other processes like deeply inelastic collisions and fission is made in the same section.

We give an overview in Table I on the physically rele-

*Also Fachbereich Physik, Freie Universität Berlin.
†Present address: Universität Marburg.

TABLE I. Dynamical parameters of the reactions studied: Energy in the laboratory system E_{lab} and in the center of mass system $E_{c.m.}$, Coulomb barrier V_B at R_B (Bass radius), wave number k, de Broglie wave length λ, Sommerfeld parameter η, reduced mass μ, and radii of the individual nuclei R_1, R_2 with $R_i = 1.28\,A_i^{1/3} + 0.8\,A_i^{-1/3} - 0.76$.

System	^{86}Kr+^{54}Fe		^{82}Se+^{56}Fe
E_{lab}(MeV)	291	310	267
$E_{c.m.}$(MeV)	112.2	119.6	108.3
V_B(MeV)	114.2	114.2	107.6
R_B(fm)	10.95	10.95	11.00
k (fm^{-1})	13.34	13.77	13.13
λ(fm)	0.075	0.073	0.076
η	80.1	77.6	77.1
μ(u)	33.1	33.1	33.2
R_1(fm)	5.07	5.07	4.99
R_2(fm)	4.29	4.29	4.35

vant parameters of the three experiments presented here: Center of mass energy ($E_{c.m.}$), Coulomb barrier (V_B), radial distance for the Coulomb barrier (R_B), and further, the wave number (k), the de Broglie wavelength (λ), the Sommerfeld parameter ($\eta = Z_1 Z_2 e^2/\hbar v$), the reduced mass ($\mu$), and the individual radii of the two nuclei (R_1, R_2; $R_i = 1.28\,A_i^{1/3} + 0.8\,A_i^{-1/3} - 0.76$) are given.

II. EXPERIMENTAL PROCEDURE

A. The kinematic coincidence setup and measurement

The experiments were performed at the VICKSI accelerator of the Hahn-Meitner-Institut using a kinematic coincidence setup [15] which is illustrated in Fig. 1. Beams for the experiments with Kr projectiles were delivered from the Van de Graaff cyclotron combination, whereas the Se beam was preaccelerated by the tandem injector. Because of the high charge states needed to bend the ions in the k = 130 cyclotron — e.g., for ^{86}Kr at E_{lab}=290 MeV a charge state of 14^+ is required — a stripping in front of the cyclotron is necessary. The low cross section of this stripping process is the limiting factor for the beam currents of about 2 pnA obtainable at the target. Targets of ^{54}Fe and ^{56}Fe, respectively, evaporated on thin carbon backings with thicknesses of 60–200 μg/cm^2, were used.

The kinematic coincidence setup is comprised of two bidimensional (x, y) position-sensitive detectors (cf. Fig. 1): (1) a detector telescope composed of a parallel-plate avalanche counter (PPAC) and a proportional counter (PC) with resistive wire anode in a first gas volume and an ionization chamber (IC) with four anode segments in a second gas volume with higher pressure; and (2) a recoil detector consisting of a bidimensional (x, y) position-sensitive and time-sensitive low-pressure multiwire chamber (MWC) [16].

The whole scattering chamber with detector telescope and recoil detector attached outside can be turned around the central point of the chamber. By turning the scattering chamber, different angle settings of the detector telescope can be obtained in steps of 5°. The MWC is mounted on a sliding flange for adjusting its position by ±140 mm without breaking the vacuum (see below). In the center of the scattering chamber a target ladder is located, which carries up to 6 targets and is attached to a vacuum lock.

The targetlike products are measured in the telescope, which has a distance of 830 mm from the target and covers an angular range $\Delta\theta_3$ of 12.2° in plane and $\Delta\phi_3$=1.45° out of plane, respectively. In the PPAC the time is measured, and the PC gives the in-plane scattering angle θ_3 with a resolution of $\delta\theta_3 < 0.1°$. The particles are then stopped in the IC, where the segmented anode allows the measurement of four successive energy-loss signals ($\Delta E1$–$\Delta E4$). The sum of all energy losses gives the

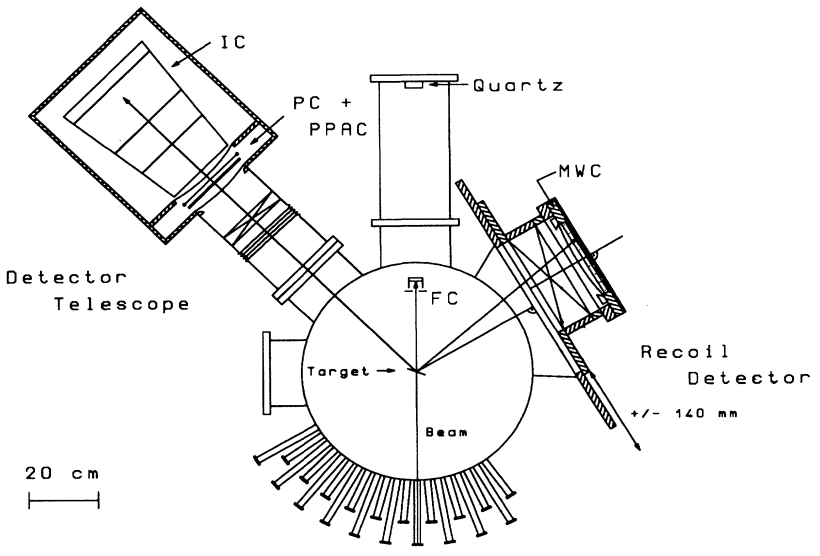

FIG. 1. Experimental set-up. The detector telescope [consisting of a parallel plate avalanche counter (PPAC), a proportional counter (PC), and an ionization chamber (IC)] and recoil detector [multiwire chamber (MWC)] are mounted on a turnable scattering chamber.

total energy deposited in the IC (E-IC), and, after correcting for the energy losses in the first stage of the telescope, the primary total kinetic energy of the detected particles. The out-of-plane angle ϕ_3 is derived from a drift time measurement started with the timing signal from the PPAC and stopped with a fast signal from the first anode segment. The energy-loss signal $\Delta E1$ depends on ϕ_3, because of an inhomogeneity of the electrical field distribution at the entrance of the IC, which leads to an incomplete charge collection. With the knowledge of ϕ_3 a correction for that effect is possible during off-line data evaluation.

The associated projectilelike nuclei were detected in coincidence in the MWC with a sensitive area of 244 mm × 122 mm, which corresponds to an angular acceptance of $\Delta\theta_4 \approx 24°$ and $\Delta\phi_4 \approx 12°$ at a distance of 590 mm from the target. The MWC contains in a symmetric setup three sensitive electrodes positioned at a distance of 3 mm; the central anode is a grid of 250 parallel gold plated tungsten wires of 12 μm diameter spaced by 1 mm, and the two outer cathodes are foils. On the cathode foils thin strips of metal are evaporated in x and y directions, with a pitch of 1 and 2 mm, respectively; these strips are connected to delay lines with 1 and 2 ns delay per tap, respectively. From the prompt anode signal the timing information is derived, and time measurements between the anode and the cathodes signals yield the orthogonal positions (x, y) and thus the in-plane and out-of-plane scattering angles θ_4 and ϕ_4, respectively.

The reactions were investigated using inverse kinematics to ensure an unambiguous Z (nuclear charge) separation over the full range of Q values for the lighter recoiling targetlike nuclei in the IC by the $\Delta E/E$ method (Fig. 2 shows an example from the measurement of ^{86}Kr on ^{54}Fe at $E_{\rm lab}$=291 MeV). The whole measured angular range was covered by three (^{86}Kr+^{54}Fe, $E_{\rm lab}$=291 MeV) and four (^{86}Kr+^{54}Fe, $E_{\rm lab}$=310 MeV and ^{82}Se+^{56}Fe, $E_{\rm lab}$=267 MeV) overlapping angle settings of the telescope, respectively. The position of the recoil detector (MWC) was adjusted for each angle setting according to the calculated two-body kinematics of the measured reaction channels.

The Q-value spectra for two-body reactions can be deduced from two independent methods: firstly, from the kinetic energy of one of the ejectiles — in the present case we measured the energy of the targetlike products in the IC (see above) — and secondly, via an in-plane angle-angle (θ_4/θ_3) correlation measurement. As an example of the first method a scatter plot of E-IC versus θ_3 for the reaction ^{54}Fe(^{86}Kr,Fe)Kr, $E_{\rm lab}$=291 MeV is shown in Fig. 3. The solid line is the result of the calculated kinematics for $E_3(\theta_3)$, including energy losses in the entrance of the detector telescope.

In Sec. II C the differences and merits of both methods for Q-value determination are discussed. The time-of-flight (TOF) difference measurement of both ejectiles could be used to deduce information on the mass of the reaction products; it is, however, not possible here, due to limitations in the mass resolution (see Sec. II C).

B. Data evaluation

As a first step of data reduction free-form gates in the scatter plots of ΔE versus E-IC were set to define the Z of the targetlike nuclei uniquely (cf. Fig. 2), i.e., for two-body reactions the nuclear charges of the associated projectilelike nuclei are also determined. With these gates different classes of exit channels — the "elastic" scattering (which contains inelastic excitations and neutron transfers) and the charge-transfer reactions of up to four protons — were defined. For these various exit channels Q-value spectra were accumulated according to the two

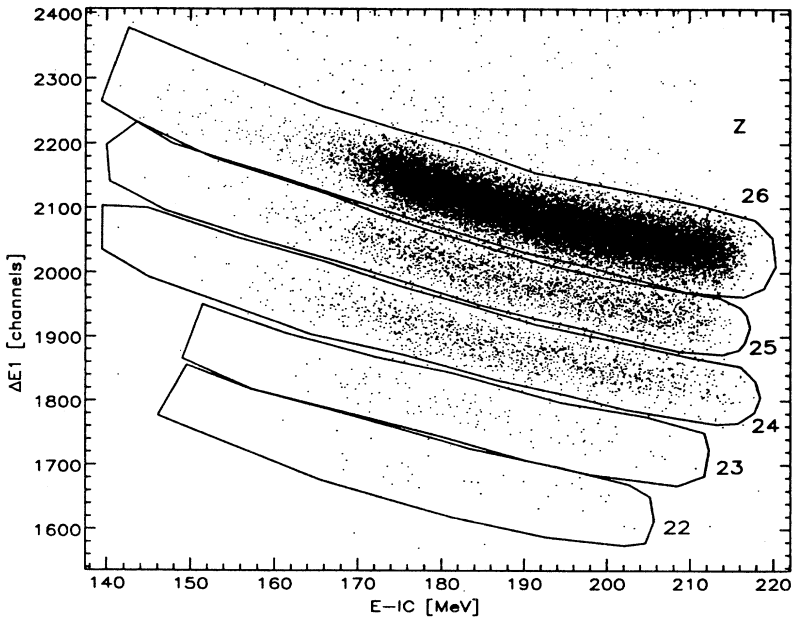

FIG. 2. $\Delta E - E$ diagram of targetlike reaction products in the Kr+Fe reaction. The charges of the reaction products are indicated (e.g., Fe, Z=26).

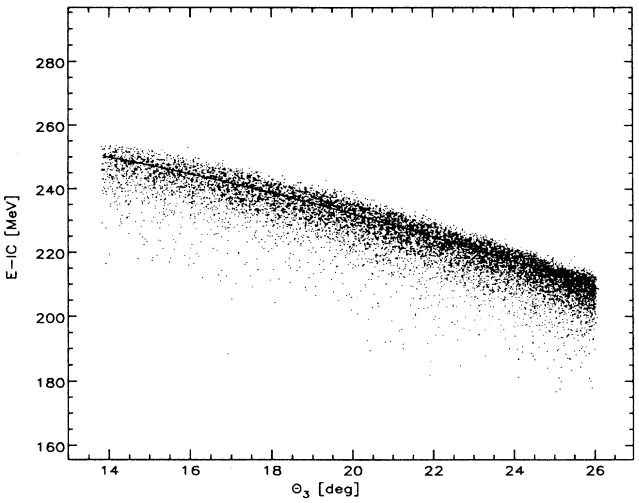

FIG. 3. Energy in the ionization chamber E-IC vs θ_3 for the reaction ^{54}Fe(^{86}Kr,Fe)Kr, E_{lab}=310 MeV.

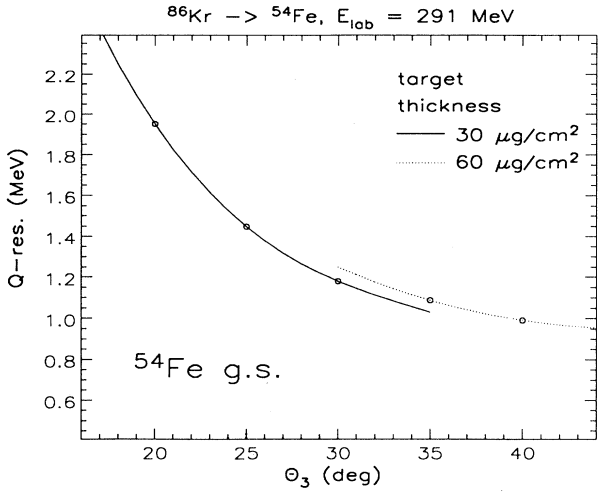

FIG. 5. Experimental energy resolution as function of the scattering angle θ_3 and target thickness for the system ^{54}Fe(^{86}Kr, Fe)Kr at E_{lab}=291 MeV.

methods mentioned above using the following procedure: Along the calculated kinematical dependence (cf. e.g., solid line in Fig. 3), the data were linearized and a projection on the ordinate yields a one-dimensional spectrum of the excitation energy over the whole angular range. If the statistics had been sufficient, cuts in the angle could have been applied to study the dependence of the excitation energy on the reaction angle. The calibration of the spectra is deduced from calculated kinematics for different excitation energies.

The angular distributions for the various exit channels are obtained from projections on the θ_3 parameter and subsequent transformations into the c.m. system employing the relevant Jacobi determinants. The absolute normalization of the cross sections was achieved with the help of the "elastic" scattering, which is identical with the Rutherford cross section at sufficiently small c.m. angles

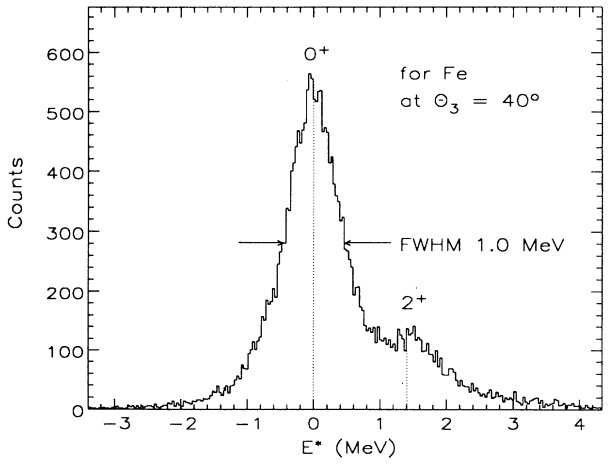

FIG. 4. Experimental energy resolution for Fe recoils from the system ^{86}Kr + ^{54}Fe at E_{lab}=291 MeV for an angle of θ_3=40°± 0.2°.

(cf. Fig. 7). Data of the different angle settings were merged to get continuous angular distributions over the whole measured angular range.

C. Discussion of experimental errors and resolutions

The Q-value resolving capability of the angle-angle correlation method is demonstrated in Fig. 4, showing the projected Q-value spectrum of the reaction ^{54}Fe(^{86}Kr,Fe)Kr, E_{lab}=291 MeV at an angle of θ_3=40°; the angular dependence of this resolution is shown in Fig. 5. The width for the ground state of ^{54}Fe, which dominates the "elastic" scattering, was measured with thin targets (30 and 60 μg/cm^2, respectively). A best value of 1 MeV is reached at an angle of θ_3=40°, but even for thin targets (30 μg/cm^2) the Q-value resolution rises to 2 MeV at θ_3=20°. Since this is insufficient to resolve individual states, target thicknesses between 180 and 200 μg/cm^2 were chosen, delivering good statistics. Using inverted kinematics, we find that generally less sensitivity in the Q-value dependent change of the correlation angles is obtained, due to the dominating velocity of the center of mass.

The extraction of Q-value spectra from the angle-angle correlation measurement is unique only for resolved masses in the exit channels, or if mass integrated spectra are dominated by one isotope only, as for the "elastic" channel mentioned above. In the present case a separation of isotopes could not be achieved from the measured TOF spectra (see below). Therefore contributions of different isotopes, corresponding to different numbers of transferred neutrons, are superimposed in the angle-angle correlation spectra with their Q-value spectra shifted heavily due to different kinematics. If, however, the E-IC information is used, the total kinetic energy (TKE) is measured directly, after correcting for energy loss both in the target and in the foils of the telescope in front of the IC. However, when extracting Q-value spec-

tra in this way, small shifts due to different kinematics of different masses must also be taken into account for superimposed energy spectra of different isotopes, which are shown in Fig. 6.

The energy scales of the Q-value spectra for the three systems presented in the following sections refer to the pure proton transfers, and the positions of the ground states of other isotopes, modified by the kinematics and reaction Q values, are labeled with the corresponding mass number (cf. Fig. 6). The experimental resolution in these spectra is about 2% (3–6 MeV) of the energy deposited in the IC.

Using a kinematic coincidence setup, we find that mass spectra can be deduced in principle from a measurement of the TOF difference between the two detectors. However, the TOF difference is not only affected by the masses in the exit channel, but also by the excitation energy. In general, the separation is worse, if inverse kinematic is used, as in the present case. The use of inverse kinematics was necessary to ensure a Z identification for the targetlike ejectiles over a large angular range. The experimental overall TOF resolution as deduced from the "elastic" channel (about 400 ps for the system ^{86}Kr + ^{54}Fe at E_{lab}=291 MeV measured with a 60 μg/cm^2 target) was due mainly to straggling effects in the target, whereas the intrinsic detector resolutions were in the order of 200 ps.

The following considerations illustrate the limits of this method: (i) the TOF difference for two adjacent isotopes (ΔA=1) is of the order of 1 ns (the values differ for different reaction Q values); and (ii) TOF difference of 1 ns will also be caused by an excitation energy difference of about 6 MeV for one isotope, which is smaller than the width of the Q-value spectra (cf. Fig. 6).

Consequently, the widths of the TOF spectra reflect mainly the excitation energy ranges. A mass information can be extracted only if a careful comparison between TOF and TKE spectra is done. In [14] we have demonstrated this procedure for the system ^{86}Kr + ^{54}Fe at E_{lab}=291 MeV and it turned out that the main contributions in the spectra belong to the pure proton transfers. This is due to the Q-value mismatch for the neutrons and the well matched Q values for proton transfer (see Table III). Although the cross section of neutron transfer rises

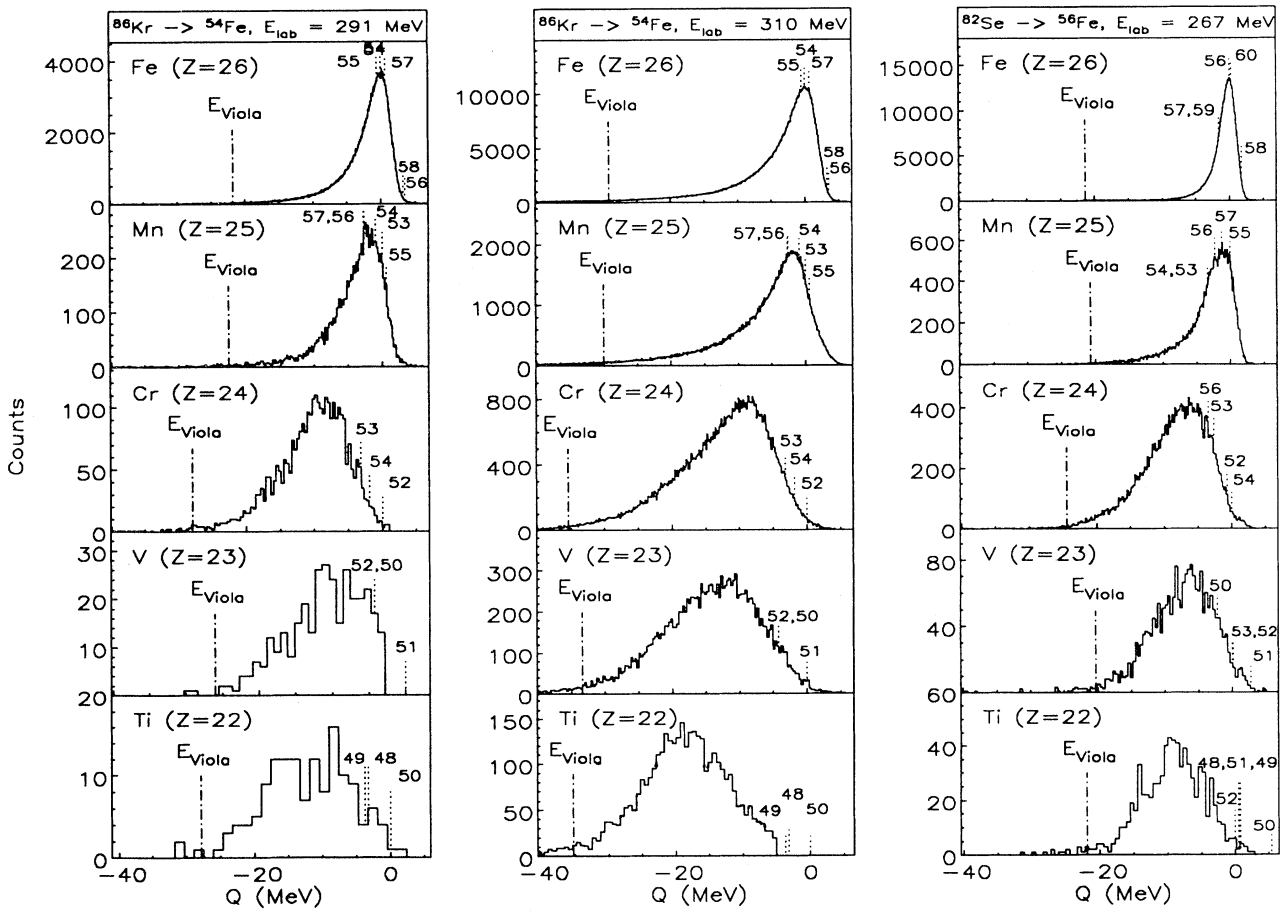

FIG. 6. Q value spectra of reaction products from the reactions of the three investigated systems from the reaction as deduced from the TKE spectra of the ionization chamber. The Q-value scales refer to pure proton transfer channels. The position of ground state Q values for different neutron transfers are marked with dotted lines and labeled with the mass number of the targetlike reaction products. The dash-dotted lines show the positions of the Viola energies.

with the energy above the Coulomb barrier, this statement holds true for the two other experiments as well. Nevertheless, no definite conclusions on the contribution of neutron transfer in the mass integrated spectra can be given.

III. EXPERIMENTAL RESULTS

A. The system ^{86}Kr+^{54}Fe

In Fig. 6 the Q-value spectra deduced from the ionization chamber signal of the targetlike recoils at a telescope angle of $\theta_{\rm lab}$=30° (this corresponds to $\theta_{\rm c.m.} \approx 120° \pm 10°$) are compared for two incident energies of ^{86}Kr ($E_{\rm lab}$=291 and 310 MeV). The spectra are shown for one proton through four-proton transfers. We observe an increasing energy loss with increasing number of transferred protons, which in the case of ΔZ=4 (reaction product Ti with Z=22) shows a distribution with a maximum yield at total kinetic energy loss (TKEL) =12 MeV for the lower incident energy, and at TKEL=20 MeV for the higher incident energy. Note that this difference in TKEL corresponds exactly to the difference in the center-of-mass incident energies (8 MeV) of the two measurements; this means that the final kinetic energy does not change. Whereas the one- and two-proton transfers can be considered to be predominantly quasielastic in the full angular range, showing in the maxima total kinetic energy losses below 10 MeV, the other reaction channels (ΔZ=3 and 4) must be considered to be to a large fraction (statistically) damped reactions, because the final kinetic energy of the maxima in the spectra is determined by the properties of the two fragments and not by the variation of the incident energy, similar to the situation in deeply inelastic reactions.

Because of limited mass and energy resolution, we define the elastic channel by the initial charge of the projectile (and target). The angular distributions of the elastic

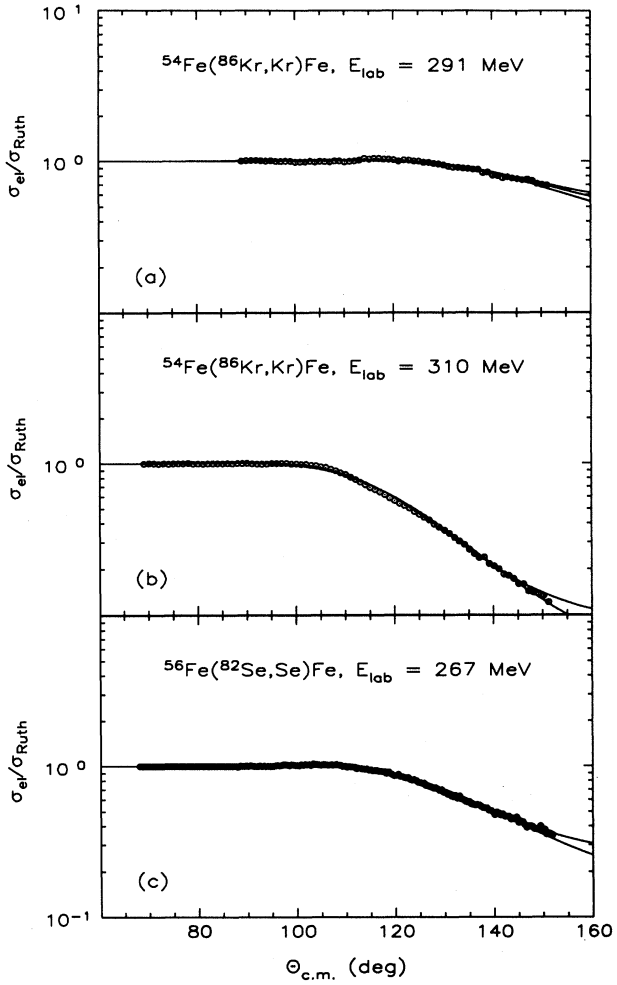

FIG. 7. Angular distributions of "elastic" scattering of the three measured systems. The curves are optical model calculations, as discussed in Sec. IV.

TABLE II. Cross sections for transfer processes and total reaction cross sections in mb for the systems ^{86}Kr+^{54}Fe at $E_{\rm lab}$=291 MeV and $E_{\rm lab}$=310 MeV, respectively, and for ^{82}Se+^{56}Fe at $E_{\rm lab}$=267 MeV. σ_R^{OM} is the total reaction cross section obtained from the optical model analysis.

	^{86}Kr+^{54}Fe		^{82}Se+^{56}Fe
$E_{\rm lab}$(MeV)	291	310	267
σ_{1p}	16.9 ± 0.5	33.8 ± 0.6	16.0 ± 0.5
σ_{2p}	8.7 ± 0.3	13.7 ± 0.2	10.9 ± 0.4
σ_{3p}	0.89 ± 0.06	2.27 ± 0.04	0.86 ± 0.01
σ_{4p}	0.23 ± 0.08	0.62 ± 0.02	0.31 ± 0.01
$\sigma_R^{\rm tr} = \sum_{i=1}^{4} \sigma_{ip}$	26.7 ± 0.8	50.4 ± 0.6	28.1 ± 0.6
$\sigma_R^{\rm OM}$	46 ± 3	289 ± 1	157 ± 2
$\sigma_{\rm fus} = \sigma_R^{\rm OM} - \sigma_R^{\rm tr}$	19 ± 3	239 ± 1	129 ± 3

scattering defined in this way (which includes minor contributions from neutron transfer and inelastic scattering) are shown in Fig. 7 for the two energies. The deviations from Rutherford scattering are rather small; for the higher energy a value of σ_{el}/σ_R of about 0.1 is reached at the largest angles. The curves shown in the figure are optical model calculations explained in the next section. The optical model potential is used for calculations of the transfer cross sections and for estimations of the reaction cross section σ_R.

The differential cross sections for the proton transfer channels are displayed in the next section together with calculated shapes of the angular distributions based on DWBA. In Table II we give the values of the integrated cross sections for one proton through four-proton transfers. In this table we notice the characteristic staggering in the relative strengths of the different transfers. The step is about a factor of 2 when going from one- to two-proton transfer and is a factor of 10 for the step from two- to three-proton transfer. This odd-even effect in the yield of the fragments is a typical effect of cold nuclear reactions; it has been observed in all three cases presented here and some other reactions [4,7] as well as in cold fission [13] and will be discussed below.

We also note that the charge (and mass) flow is in the direction of *increasing mass asymmetry*, in contrast with the expectations for a completely equilibrated system; this would show a drift to two fragments of equal mass, because for the Z^2/A value of the total system ($A \approx 140$) with some angular momentum the initial mass asymmetry is well beyond the Businaro-Gallone transition point [17,18]. The reason for the transfer of charge and mass to larger asymmetry is the fact that cold multinucleon transfer reactions (or quasielastic reactions) proceed along regions of optimum Q values. For discussion of the optimum Q values we refer readers to Refs. [4,22]. The large span of quasielastic reactions is observed here, because the system was chosen in order to have optimum Q values for up to four-proton transfer in the observed directions. The relevant Q values are given in Table III.

B. Results for the system ^{82}Se+^{56}Fe

This system was measured in a similar way as the previous one at an incident energy at the nominal Coulomb barrier (see Table I). The energy spectra from the ionization chamber are also shown in Fig. 6. They have great similarity with the result from the ^{86}Kr+^{54}Fe system. We note, however, that the width of the spectra is somewhat narrower, and the energy loss (measured from the incident energy) is smaller. The latter fact is mainly due to the more negative Q values of the present reactions, e.g., the difference for the four-proton transfer between the two cases (see Table II) is approximately 5 MeV. Therefore less energy (5 MeV) is available for "excitation" or energy loss (in terms of deformation) in the case of ^{82}Se+^{56}Fe, as compared to ^{86}Kr+^{54}Fe.

The result of the "elastic" scattering (which contains neutron transfer and inelastic excitations) is shown in Fig. 7. The shape of the σ_{el}/σ_R curve places this system at a relative energy to the barrier, which is intermediate between the two energies of the ^{86}Kr + ^{54}Fe systems.

The odd-even effect in the element yield (see also Table I) and the charge flow to larger asymmetry (against the statistical driving force) are both strong indications for a cold quasielastic multinucleon transfer just as in the case of ^{86}Kr + ^{54}Fe.

C. Energy loss spectra

For a discussion of the mechanisms of mass and charge transfer, it is very instructive to compare the energy spectra with predictions from the energy systematics of binary reactions, which are completely relaxed, known as the Viola systematics [19,20]. For a discussion of the observed energy loss we define in Fig. 8 on a linear energy scale the following quantities: $E^0_{c.m.}$, center-of-mass energy of the reaction product (for Q_{00}= 0 MeV); Q_{00}, ground state Q value of the reaction; $\overline{E}_f$, most probable final energy (in the c.m. system); $\overline{E}^*$, most probable

TABLE III. Ground state Q values of one-proton up to four-proton transfer (± two-neutron transfer) in the systems ^{86}Kr+^{54}Fe and ^{82}Se+^{56}Fe.

			^{86}Kr+^{54}Fe		
	$2n$	$1n$	$0n$	$-1n$	$-2n$
$+1p$	−1.159	−5.697	−6.880	−15.864	−22.993
$0p$	3.552	−0.558	0.000	−7.863	−11.495
$-1p$	0.361	−1.215	−0.233	−6.209	−9.560
$-2p$	1.936	0.645	3.819	−1.855	−3.313
$-3p$	−4.652	−3.779	0.389	−3.805	−5.209
$-4p$	−6.423	−4.917	0.638	−3.062	−2.569
			^{82}Se+^{56}Fe		
	$2n$	$1n$	$0n$	$-1n$	$-2n$
$+1p$	−2.335	−6.191	−6.323	−12.084	−14.294
$0p$	1.714	−1.630	0.000	−5.380	−5.007
$-1p$	−2.735	−3.793	−1.480	−4.868	−4.906
$-2p$	−2.318	−3.111	1.162	−1.440	0.477
$-3p$	−10.006	−8.565	−4.189	−4.017	−1.408
$-4p$	−12.130	−10.271	−4.219	−3.598	1.142

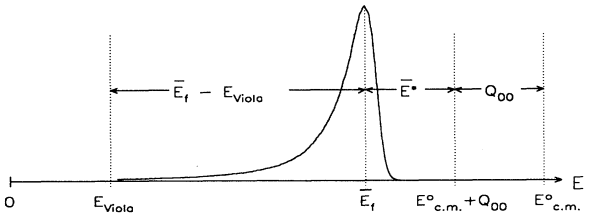

FIG. 8. Definition of quantities in the energy spectra for a comparison with the energy of completely damped reactions ($E_{\rm Viola}$). $\bar{E}_f$ is the most probable final energy of the fragment and Q_{00} is the ground state Q value.

excitation energy of the fragments (total kinetic energy loss).

The kinetic energy of fission fragments has been analyzed by Viola [19], and it has been found that the final energy corresponds to a completely relaxed system, where the kinetic energy is determined by the Coulomb energy of the two fragments at the scission point. The systematics have been extended for asymmetric mass splits by Wilcke *et al.* [21] and was reevaluated by Viola, including more recent data [20]. The result is the following expression for the energy of two separating fragments:

$$E_{\rm Viola} = \left(0.1189\frac{Z^2}{A^{1/3}} + 7.3\right)\frac{4Z_1Z_2}{(Z_1+Z_2)^2}\ \text{MeV} \quad . \quad (1)$$

The distance of $\bar{E}_f$ from the value of $E_{\rm Viola}$ can be taken as a measure of relaxation in the reaction. The energy spectra in Fig. 6 have maxima well above $E_{\rm Viola}$, however, the spectra extend down to the value given by $E_{\rm Viola}$ in the case of reactions with three- and four-proton transfers. In these cases also the spectra at different reaction angles could be discussed, however, the small absolute counting rate accumulated for these cases does not allow such a discussion, nor a decomposition into quasielastic (main) and completely relaxed components.

In Fig. 9 we give a systematic survey of the difference of $\bar{E}_f - E_{\rm Viola}$ and of the kinetic energy loss $\bar{E}^*$ observed in the three cases. We remark that the main part of the spectra can be attributed to quasielastic reactions. After the transfer of four protons the dominant part of the reactions, as seen in the energy spectra (which is angle integrated) corresponds to excitations of both fragments of not more than 10 MeV. We want to point out that with the increase of the incident energy for the case of ^{86}Kr+^{54}Fe, the value of $\bar{E}_f - E_{\rm Viola}$ grows and the excitation energy in the fragments stays constant. This indicates that the same configurations are populated in the fragments at the two energies. For the ^{82}Se+^{56}Fe case the energy loss (or excitation energy of the fragments) appears even smaller; we interpret this result as being due to the more negative Q values in this case, which in fact leaves even less energy for intrinsic excitation, as mentioned in Sec. II B.

The overall picture from these energy spectra is that the main cross section of the reaction is not relaxed or not thermalized in all degrees of freedom; the fragments stay rather cold. However, the energy loss observed is in the range of 10–15% of the center-of-mass energy or the energy of the Coulomb barrier (which is the same). This indicates that the final fragments are separated by a distance which is 1.0–1.5 fm larger than the distance in the incident channel. In order to keep nuclear contact the fragments must thus be deformed, creating a dinuclear complex such as that in deeply inelastic reactions [2,3]. Further consideration of this point will be given in Sec. V.

IV. ANALYSIS OF THE DATA

In this section we use semiclassical considerations as well as DWBA (first order transfer perturbation approach) in order to study the reaction mechanism and to have a background relative to which deviations can be discussed in terms of the formation of a dinuclear complex.

A. Semiclassical description

In the semiclassical model the differential cross section for transfer $d\sigma_t/d\Omega(\theta)$ is factorized in three parts

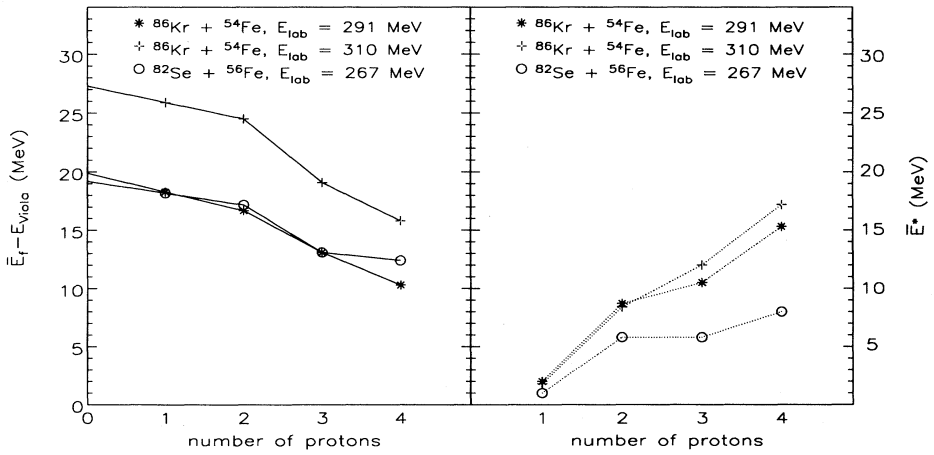

FIG. 9. Difference of the experimentally observed average final energy and the energy expected from Viola systematics, and total kinetic energy loss (excitation energy) of fragments for the three cases.

$$\frac{d\sigma_t}{d\Omega}(\theta) = \frac{d\sigma_{\rm el}}{d\Omega}(\theta) P_t(\theta) F(Q). \quad (2)$$

The underlying concepts are extensively discussed in Refs. [4] and [22]. We use here for the elastic scattering $d\sigma_{\rm el}/d\Omega$ the measured cross section, which deviates from Rutherford scattering at smaller distances of closest approach (see below). The matching factor $F(Q)$ is close to unity in our case (see Ref. [22]), and can be neglected, because the reactions studied here are sufficiently well matched. $P_t(\theta)$ is the transfer probability. Equation 2 holds even when the "elastic" cross section (with inelastic excitations and neutron transfers) is used, provided the transfer cross section is defined in the same manner, as the "elastic" channel.

The approach is based on classical orbits, determined mainly by the Coulomb field but possibly with small modifications due to the attractive nuclear force. The angle information is transformed to the distance of closest approach $R_{\rm min}$ by calculating the classical trajectories. This quantity is replaced by the overlap parameter d_0 [$d_0 = R_{\rm min}/(A_1^{1/3} + A_2^{1/3})$], which allows a comparison of different systems independent of their sizes (see also Ref. [22]).

The elastic scattering cross section can be written as a product of an absorption function ($1-P_{\rm abs}$) and the Rutherford cross section: $\sigma_{\rm el}(\theta) = [1 - P_{\rm abs}(\theta)]\sigma_{\rm Ruth}(\theta)$. In Fig. 10 we show plots of $\sigma_{\rm el}/\sigma_{\rm Ruth}$ as function of d_0, which represent the absorption function.

Figure 10(a) shows the result for the "elastic" scattering in the system ^{86}Kr+^{54}Fe at $E_{\rm lab}$=310 MeV for two cases of determining d_0: one where only the Coulomb interaction is considered, and a second one with the assumption of an additional nuclear potential, which was derived from an optical model analysis presented in the next section. We find a small but distinct influence of the attractive nuclear potential at $\theta_{\rm c.m.} > 120°$ (values of d_0 below 1.55 fm), i.e., at the "backward" angles. Figure 10(b) shows a comparison of the absorption curves of the two systems ^{86}Kr+^{54}Fe and ^{82}Se+^{56}Fe with the inclusion of the real optical potential in the calculation of d_0. The two curves coincide within the experimental errors. This is not the case if the nuclear potential is not taken into account in the calculations.

Although the definition of the final channel with respect to Q value and mass is not as precise in this work as in Ref. [4], where a magnetic spectrometer was employed, we use for a quantitative discussion the recipe defined by Eq. (2) to calculate the transfer (probability) functions P_t. We do this because systematic features of transfer processes are more easily seen in the representation of transfer probabilities. These are shown in Fig. 11 for the three systems. There are several observations from this representation which help in the interpretation of the reaction mechanism.

(1) *Slopes.* The exponential decrease of P_t as function of d_0 should reflect the behavior of the DWBA-form factor (see Ref. [4]). We find that in the two ^{86}Kr+^{54}Fe cases the two-proton transfers show a slope which is twice as steep as for the one-proton transfers. This is a result, which is expected for the transfer of a proton *pair*, with approximately twice the binding energy of one proton ($2E_B$) or for a sequential transfer of two protons. For the three- and four-proton transfers the average slopes (also for the two-proton transfer in the case of ^{82}Se+^{56}Fe) seems to be the same and does not vary any more with the number of transferred protons. Thus in our case only the results for one- and two-proton transfers are consistent with a quasielastic transfer process. Actually, a Q-value window for the two-proton transfer with Q values smaller than 15 MeV gives less steep slopes than that shown in Fig. 11. The average excitation energy is rather small (see Fig. 9) and the energy loss is still far away from the Viola systematics (cf. Fig. 6), therefore a separation into quasielastic and deeply inelastic reactions is not meaningful. The reactions have rather the properties of a cold reaction, and a clear odd-even staggering is observed (which is discussed in the following quantitatively).

(2) *Odd-even staggering.* In the two cases (^{86}Kr+^{54}Fe,

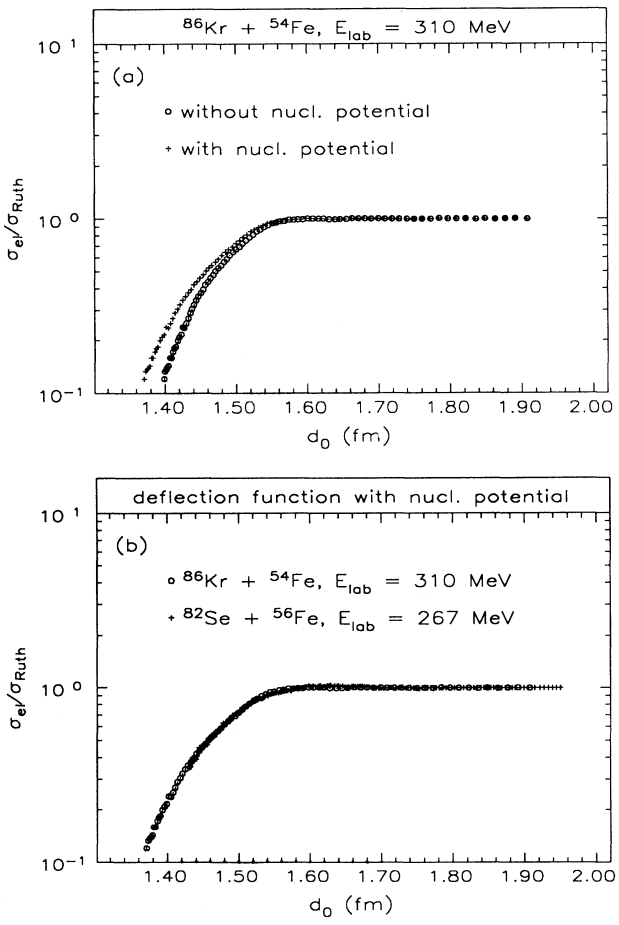

FIG. 10. Absorption functions ($\sigma_{\rm el}/\sigma_{\rm R}$) as function of the overlap parameter d_0. (a) For the system ^{86}Kr+^{54}Fe at $E_{\rm lab}$=310 MeV; d_0 has been calculated with two assumptions. In the second case in addition to the Coulomb potential a nuclear potential is included in the calculation of d_0. (b) Comparison of the absorption functions for ^{86}Kr+^{54}Fe at $E_{\rm lab}$=310 MeV and ^{82}Se+^{56}Fe at $E_{\rm lab}$=267 MeV; the two data sets become indistinguishable once the nuclear potential is included.

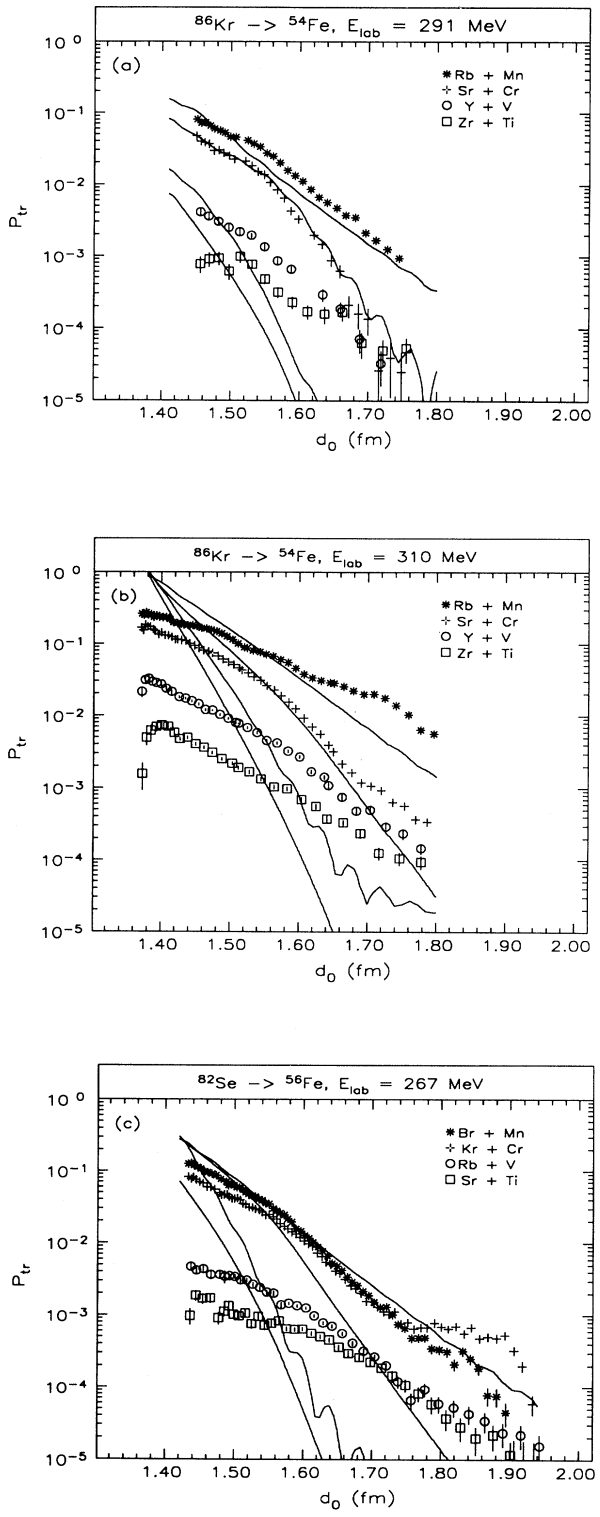

FIG. 11. Transfer functions (probabilities) obtained by dividing the transfer cross section by the measured (or calculated) elastic cross section as function of the overlap parameter d_0. The calculated curves are normalized to a common point corresponding to the concept of a sequential transfer. (a) ^{86}Kr+^{54}Fe, $E_{\rm lab}$=291 MeV. (b) ^{86}Kr+^{54}Fe, $E_{\rm lab}$=310 MeV. (c) ^{82}Se+^{56}Fe, $E_{\rm lab}$=267 MeV.

$E_{\rm lab}$=291 MeV; ^{82}Se+^{56}Fe, $E_{\rm lab}$=267 MeV) which have the lowest energy with respect to the Coulomb barrier, there is a pronounced enhancement of the two- and four-proton transfers. Thus the steps in the probability from one to two and from three to four protons are much smaller than the previous steps, which reflect the probability to transfer the first and the third proton, respectively. This is a clear indication of a cold reaction, where pairing plays an important role. Observations of this effect for proton transfer are discussed in Refs. [4,7].

The solid curves in Fig. 11 are results of DWBA calculations explained in the next section. They are obtained from the division of the calculated transfer cross section by the "elastic" cross section and transforming $\theta_{\rm c.m.}$ to d_0, just as done with the experimental data. The normalization of the calculated curves to the experimental data was determined in the representation as angular distributions, where both were matched in the region of the grazing angles. The calculated curves show the expected increase of the slopes with increasing number of transferred nucleons (protons). The deviations of the experimental data from these expectations are discussed in the representation of the data as angular distributions in the next section.

B. DWBA analysis of the multiproton transfer

In view of the fact that for the discussion of the rotation of a dinuclear complex the observation angle is the relevant quantity, we turn back to the discussion of the angular distributions. The analysis of the shapes of the angular distributions is done using a standard DWBA analysis as described for example in Ref. [4]. The distorting potentials are obtained from the optical model fit to the "elastic" scattering. The present calculations for the "elastic" scattering data are very insensitive to the choice of the real potential. In Table IV we give different sets of Woods-Saxon parameters fit to the measured "elastic" scattering of the system ^{86}Kr+^{54}Fe at $E_{\rm lab}$=291 MeV. All four parameter sets describe the measured data equally well. For the transfer reactions with a steep form factor (such as two-proton transfer) a stronger sensitivity is expected, because the real potential changes the deflection function (i.e., the determination of the minimum distance) as illustrated in Fig. 10(a). This is in fact observed, as shown in Fig. 12. For the form factors we use the standard procedure of calculating the bound states with known quantum numbers and binding energies (see Ref. [4]).

The two-proton transfer turns out to be quite sensitive to the choice of the optical potential. Figure 12 shows two examples. Figure 12(a) shows the result for the (Kr,Sr) reaction at $E_{\rm lab}$=291 MeV. The potential A (see also Table IV) certainly has to be favored. At the higher Kr energy [cf. Fig. 12(b)] another problem arises at the largest angles (smallest distances); the absorption appears to be too weak in the calculation, whereas the experimental data show a fall-off. The calculation gives a cross section which continues to rise. A possible way to fit the data is an increase of the real potential strength

TABLE IV. Woods-Saxon parametrizations of the optical potential for the system ^{86}Kr+^{54}Fe at E_{lab}=291 MeV for a fit to the "elastic" scattering. The asterisks denote numbers that were fixed during the fit.

Potential	V(MeV)	r_{0r}(fm)	a_r(fm)	W(MeV)	r_{0i}(fm)	a_i(fm)
A	11.2	1.38	0.5*	0.33	1.45*	0.4*
B	3.3	1.48	0.3*	0.24	1.50*	0.3
C	37.0	1.24	0.6*	127.0	1.24*	0.3
D	18.2	1.34	0.6*	2.8	1.22*	0.6

in the exit channel. The effect is shown in Fig. 12(b), where the strength of the real potential in the exit channel has been varied. With this approach in fact a better agreement can be achieved. This indicates that already in the one- and two-proton transfer channels some approximations (namely, the specific choice of the exit channel distortion potential equal to that one of the incident channel) used in the DWBA calculations are not valid. Thus the potential in the final channel had to be adjusted and turns out to be quite different from that of the incident channel.

For a further discussion of the angular distributions the one- through four-proton transfers have been calculated and the shapes are compared with the experimental data. The shape of the angular distributions of multinucleon transfer is governed in the DWBA approach at energies close to the barrier [4] by the steepness of the corresponding form factor (this is sometimes represented by a transfer probability as function of the minimum distance). The sequential nature of the multinucleon transfer does not influence this property, because interference effects due to intermediate steps are negligible at backward angles, but changes mainly the absolute value (the sequential transfer process dominates by typically two orders of magnitude); actually, each step in the sequential process is so weak as to be consistent with the Born approximation. A coupled reaction channel study for multiple neutron transfer done in Ref. [8] illustrates this point.

This comparison is shown in Fig. 13, where for all three systems the experimental data are shown together with the DWBA calculations. The latter are normalized to a point which is typically at $\theta_{c.m.}$=105–140°. The rising slope at smaller angles is generally well reproduced for the one-proton transfer and in the case of Kr+Fe also for the two-proton transfer. The fall-off of the calculated curves at larger angles is generally strongly underestimated, unless much more absorption or attraction is introduced in the exit channel.

The discrepancies among the DWBA predictions at the smallest angles cannot be removed by changes in the scattering potential nor by changes in the form factors because these angles correspond to rather large distances, where only Coulomb interaction along the scattering orbit occurs. The difference between the experimental data and the normalized DWBA calculations in this forward angular range as shown in Fig. 13 is interpreted as being due to another reaction mechanism: the decay of a two-center complex (see Sec. V). This behavior seems to be unusual and possibly specific to the systems (and incident energies) studied here. There exists a variety of experimental examples [4,7], where at least in the very restricted angular range, which has been measured, the multiproton transfer shows angular distributions and transfer functions, which are in agreement with a multistep DWBA approach.

C. Overview of the cross sections

Using the normalized DWBA calculation we can obtain the integrated cross sections for the transfers con-

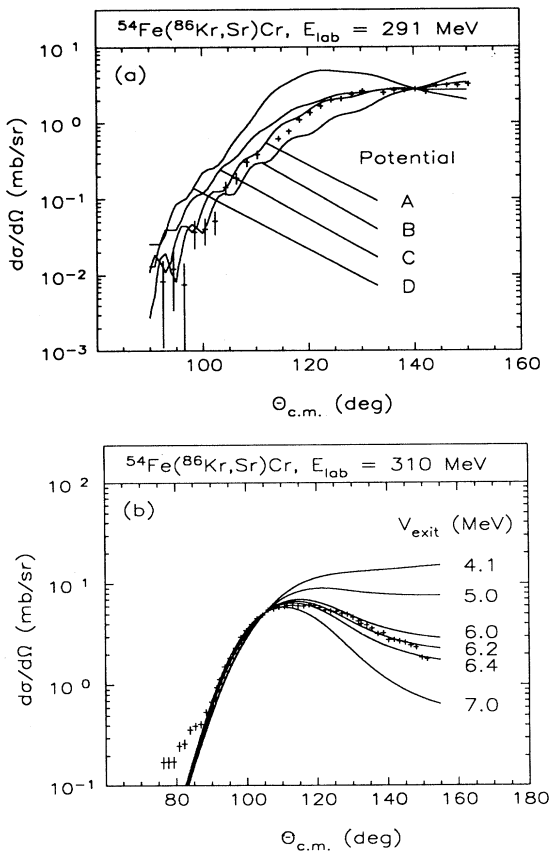

FIG. 12. DWBA prediction for two-proton transfers ^{54}Fe(^{86}Kr,Sr)Cr. (a) Illustration of the variations of the real potential on the two-proton transfer calculations at an incident energy of 291 MeV. (b) Changes of the optical potential in the exit channel of the two-proton transfer reaction at E_{lab}=310 MeV. Incident channel potential: V = 4.1 MeV, r_{0r} = 1.38 fm, a_r = 0.5 fm.

sidered as quasielastic processes (cf. Table I). The total reaction cross section σ_R is obtained from the optical model fit. We are thus able to make a decomposition of the total reaction cross section σ_R into $\sigma_{\rm DWBA}$ (quasielastic cross section), $\sigma_{\rm ND}$ ("two-center complex" cross section, nondirect), and $\sigma_{\rm fus}$. Thus the difference between σ_R and the rest we can call fusion cross section: $\sigma_{\rm fus} = \sigma_R - \sigma_{\rm DWBA} - \sigma_{\rm ND}$. We plot these quantities for the three systems as function of the energy above the barrier in Fig. 14. We find a systematic behavior which shows that for the quasielastic reactions ($\sigma_{\rm DWBA}$ and $\sigma_{\rm ND}$) a saturation has been reached in contrast to the fusion reaction which is rising continuously.

V. THE DINUCLEAR COMPLEX

In close resemblance to the formation of an (excited) dinuclear complex in deeply inelastic collisions [3] we will discuss in this section the formation of a dinuclear complex which is cold; the fragments have rather small excitation energies defined by a total energy loss of only 10–15 MeV. This leaves 5–8 MeV for each fragment; in addition it must be assumed that they are strongly deformed, because nuclear contact could not be kept otherwise for fragments with energies 15% smaller than the Coulomb barrier.

The excitation energy is most likely absorbed into deformation of the fragments, and we will consider the decay of a dinuclear complex into two deformed fragments. The angular distributions show in the range of angles from $\theta_{\rm c.m.}$=70–100° a slope in $d\sigma/d\Omega(\theta)$ which is very similar for all cases: we observe an exponential decay which varies by a factor of 2 within the statistical errors. For the decay of a dinuclear complex, $d\sigma/d\theta$ must be considered here; however, in the relation $d\Omega = \sin\theta d\theta d\phi$ the

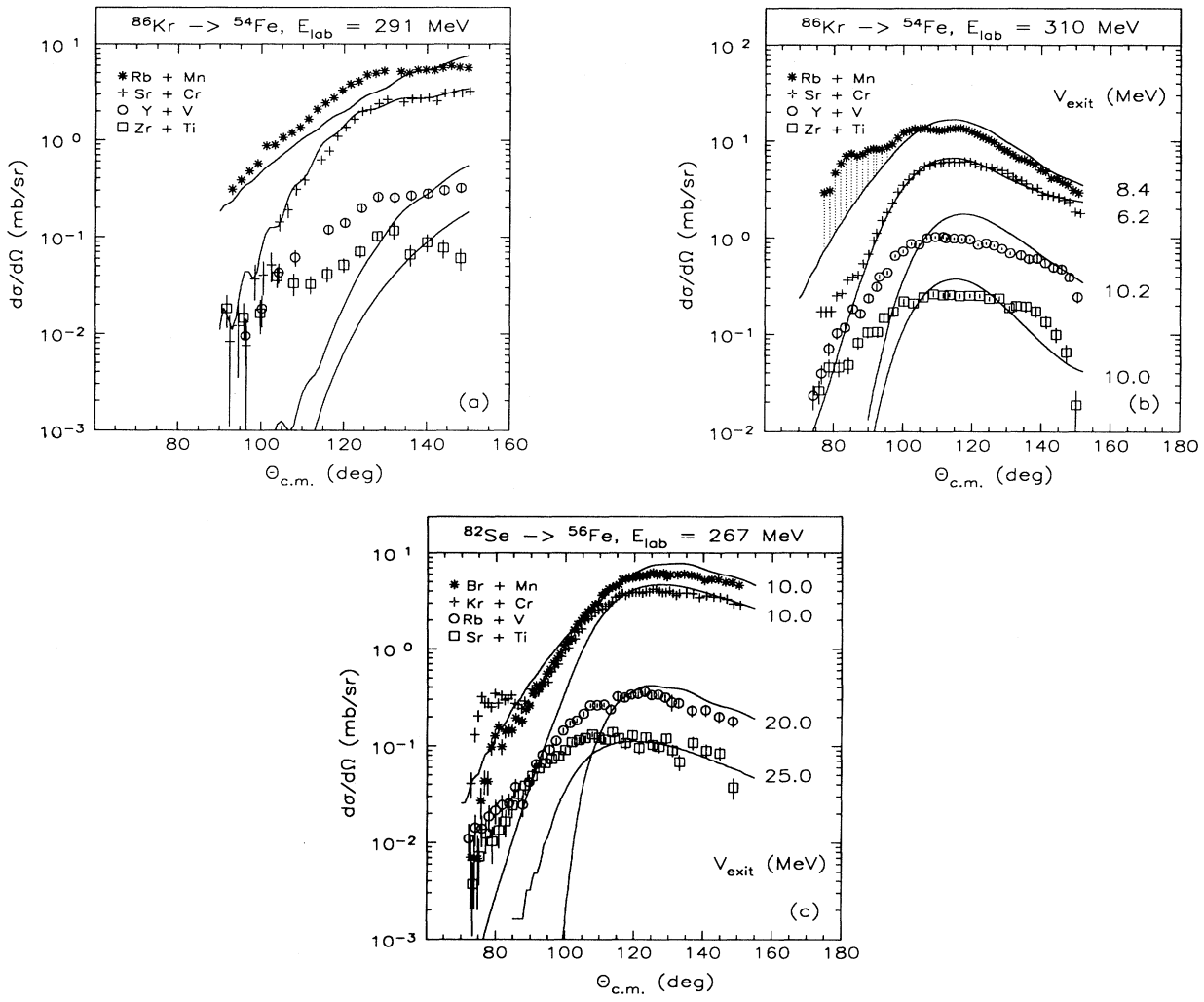

FIG. 13. Angular distributions for one-proton through four-proton transfers for the three systems. The curves are DWBA calculations normalized as indicated in each case. (a) ^{86}Kr+^{54}Fe at $E_{\rm lab}$=291 MeV. The curves are normalized at $\theta_{\rm c.m.}$=140°. (b) ^{86}Kr+^{54}Fe at $E_{\rm lab}$=310 MeV. The curves are normalized at $\theta_{\rm c.m.}$ = 105°. The exit channel real potential strength was adjusted as indicated by choosing a different depth V_0. (c) ^{82}Se+^{56}Fe at $E_{\rm lab}$=267 MeV. The DWBA curves are normalized at $\theta_{\rm c.m.}$=117° the real potential in the exit channel has been adjusted.

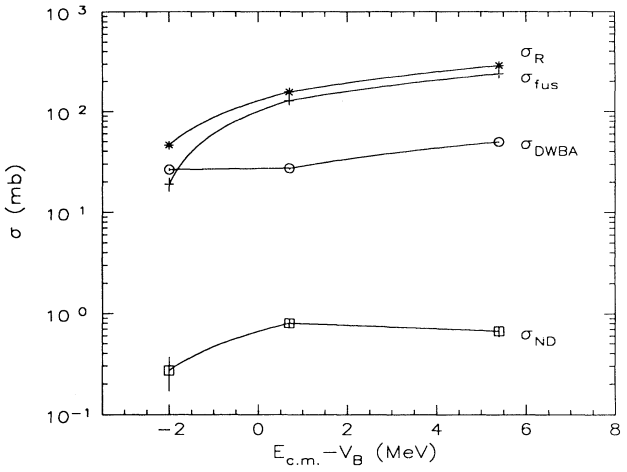

FIG. 14. Cross section for the ^{86}Kr+^{54}Fe and ^{82}Se+^{56}Fe systems as function of the incident energy above the barrier. σ_R, total reaction cross section; $\sigma_{\rm fus}$, fusion cross section; $\sigma_{\rm DWBA}$ and $\sigma_{\rm ND}$ stand for the direct transfer and nondirect cross sections, respectively.

additional variation from the factor $\sin\theta$ in the relevant angular region is only 6%.

In Fig. 15 we give a pictorial view of the angular distributions obtained for a dinuclear complex formed in a transfer reaction. If a dinuclear complex is formed after the transfer of some nucleons it will start to decay from an angular position at the grazing angle; it will decay while continuing to rotate, as suggested in Fig. 16. The exponential decay in the forward angular region is obtained by rotation of the complex with lifetime τ as discussed below.

A. Lifetime of a dinuclear complex

If we assume that we observe the decay of a dinuclear complex which rotates, we write for the angle of rotation

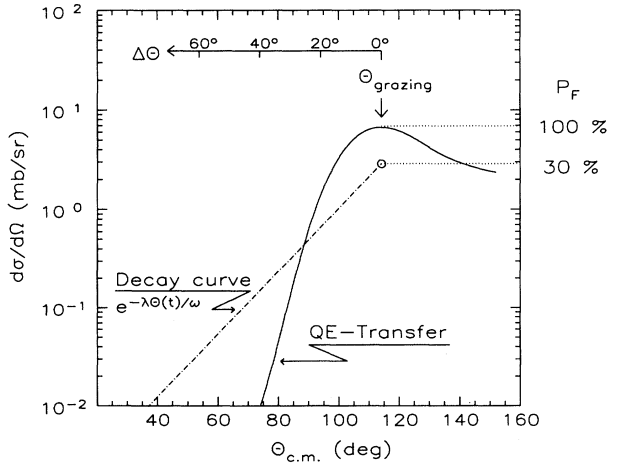

FIG. 15. Illustration of the exponential decay of a dinuclear complex formed with a probability of 30% at the grazing peak of the quasielastic reaction.

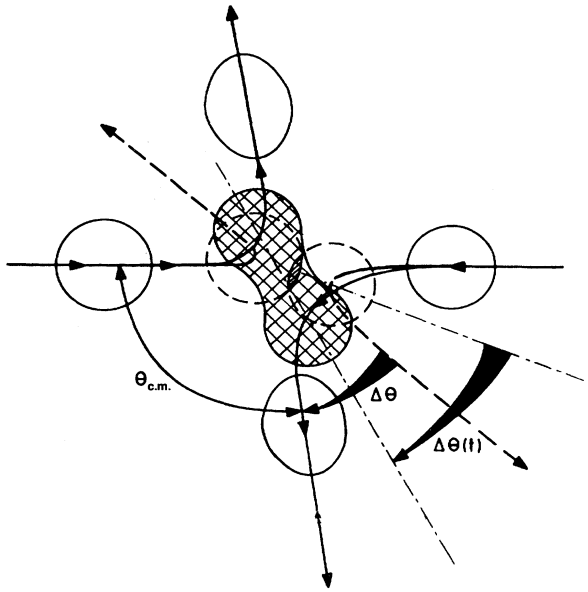

FIG. 16. Pictorial view of the nuclear reaction which leads to sticking, the formation of a dinuclear complex, and its decay over the rotation angle $\Delta\theta$. The incident energy corresponds to a nuclear contact for scattering orbits leading to reaction angles $\theta_{\rm c.m.} > 120°$.

$\theta(t)$ with the angular velocity ω (or frequency $2\pi\nu$)

$$\theta(t) = \omega t = 2\pi\nu t. \tag{3}$$

After rotation by an angle interval $\Delta\theta$ we observe a (exponential) decay by the factor F (with the decay constant λ) in the time interval Δt

$$F(\Delta t) = \exp\left(-\frac{\lambda}{\omega}\Delta\theta\right) = \exp\left(-\lambda\Delta t\right). \tag{4}$$

In order to determine the decay constant λ, or the mean lifetime $\tau = 1/\lambda$, we have to calculate the angular velocity ω. We obtain this from the expression for the rotational energy $E_{\rm rot}$

$$E_{\rm rot} = \frac{1}{2}J\omega^2 = \frac{I(I+1)\hbar^2}{2J} \approx \frac{I^2\hbar^2}{2J}. \tag{5}$$

Here I is the angular momentum and J the moment of inertia. The final expression to determine τ from the exponential decay over an angular interval $\Delta\theta$ thus reads

$$\tau = \frac{\Delta\theta}{\ln(1/F)\omega} = \frac{\Delta\theta}{\ln(1/F)}\frac{J}{I} \quad 1.574\times10^{-23}\ \text{s}\ . \tag{6}$$

For the determination of τ from the observed exponential decays we have to use values of J and I relevant for the present case. We assume that the critical angular momentum for fusion gives approximately the angular momentum for the dinuclear complex. They can be obtained from the cross section for fusion, which have been determined in Sec. IV, applying the sharp cutoff model.

For the moment of inertia J we take two deformed fragments (deformation parameter δ) with an internuclear distance $R_0 = d_0(A_1^{1/3} + A_2^{1/3})$ and d_0=1.55 fm, a

value which reproduces approximately the observed energies in the exit channel:

$$J = \frac{2}{5}M_1R_1^2\left(1+\frac{1}{3}\delta_1\right) + \frac{2}{5}M_2R_2^2\left(1+\frac{1}{3}\delta_2\right) + \frac{A_1A_2}{A_1+A_2}R_0^2. \quad (7)$$

With these assumptions we can draw curves for the lifetime τ of a dinuclear complex as function of the factor F for different values of angular momentum I according to Eq. (6). They are shown in Fig. 17(a) for the system ^{86}Kr+^{54}Fe, 310 MeV and in Fig. 17(b) for ^{82}Se+^{56}Fe, 267 MeV.

B. Results for the lifetime of the dinuclear complexes

In Fig. 17 the hatched areas indicate the regions of values of F, which were derived from the experimental data shown in Fig. 13 for an angle interval of $\Delta\theta$=30°. The slopes of the cross sections at small c.m. angles show little dependence on the number of transferred protons within the statistical errors, at least for the two-, three-, and four-proton transfers. This situation occurs, as schematically shown in Fig. 15, if the cross section of the quasielastic transfer in the chosen angular range is much lower than that one of a second process, namely, the decay of a dinuclear complex, indicated by the decay curve. In Fig. 17 the dependence of the lifetimes on the angular momentum I of the composite system is also shown. A good estimate for the maximum value of I is given by the critical angular momentum l_{crit} in a sharp cut-off approximation for the fusion cross section. These values — 38$\hbar$ for the system ^{86}Kr+^{54}Fe, 310 MeV and 27$\hbar$ for ^{82}Se+^{56}Fe, 267 MeV — are also obtained in the DWBA calculation as partial waves with the maximum cross section, e.g., for the two-proton transfer. However, from the present experimental data it is not possible to fix uniquely the most probable l value of the dinuclear system. Therefore we have plotted in Figs. 17(a) and 17(b) lifetime curves for the maximum angular momenta, which yield the shortest lifetimes, and for some lower values of l. Because various studies [25] have shown that close to the barrier the l-value distribution for compound nucleus formation is smeared out considerably (relative to the distribution calculated with the sharp cut-off model), we choose l=20$\hbar$ as a mean value. The range of possible angular momenta around this mean value gives the range of the extracted lifetimes τ. The uncertainties from the errors in the determination of the decay factor F from the slopes of the angular distributions at small c.m. angles [shown as hatched areas in Figs. 17(a) and 17(b)] are much smaller than the resulting ranges.

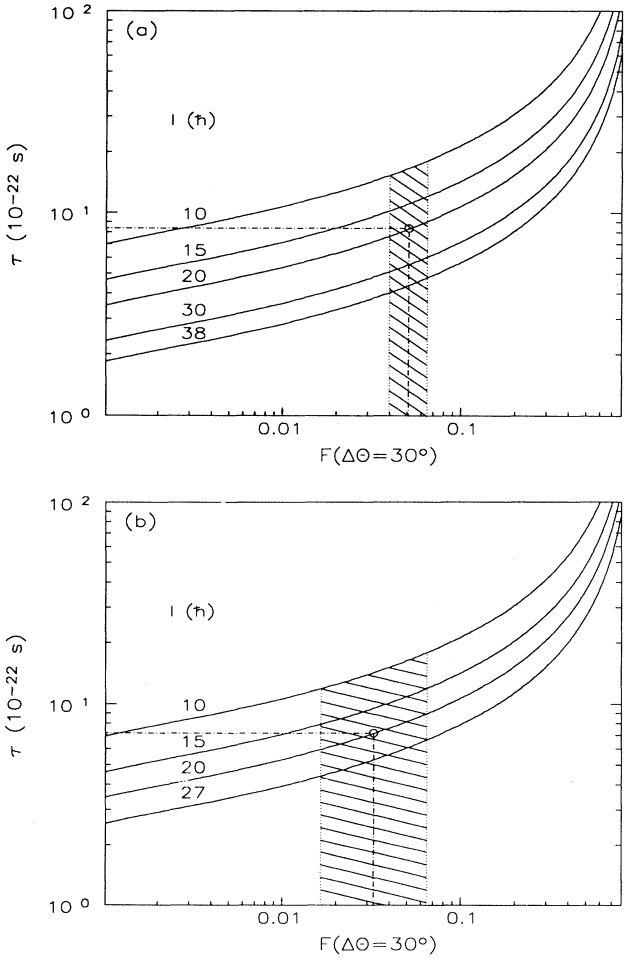

FIG. 17. Results for lifetime τ of the dinuclear complex deduced from the decay factor F over an angular range of 30° and for different total angular momenta I: (a) for ^{86}Kr+^{54}Fe at E_{lab}=310 MeV; (b) for ^{82}Se+^{56}Fe at E_{lab}=267 MeV.

The resulting values for the lifetimes are $\tau=8^{+3}_{-4}\times10^{-22}$ s for ^{86}Kr+^{54}Fe at E_{lab}=310 MeV and $\tau=6^{+5}_{-2}\times10^{-22}$ s for the system ^{82}Se+^{56}Fe at E_{lab}=267 MeV, respectively.

Finally we want to discuss the fusion reaction as a process, which could possibly contribute to the observed nondirect cross section σ_{ND} besides the decay of the dinuclear system. For this discussion the system ^{86}Kr+^{54}Fe at E_{lab}=310 MeV is chosen, because it has the largest fusion cross section of σ_{fus}=239 mb out of the three investigated systems (cf. Table I). The maximum angular momentum of the compound nucleus (^{140}Sm for this system) as given in Ref. [24] is about 75$\hbar$. Therefore, fission is expected to be negligible. The excitation energy of the compound nucleus is given by the difference between the incident energy and the Q value for complete fusion. Taking into account a rotational energy of 8 MeV yields an excitation energy of E^*=36 MeV.

Nevertheless we give a quantitative estimate of the fission component. The compound nucleus ^{140}Sm is well below the Businaro-Gallone point and if it fissions it will fission symmetrically with fragments masses of $A_{ff}\approx$70. To estimate the probability of fission as exit channel in the present system we applied the statistical model of Vandenbosch and Huizenga [23] and obtain $\Gamma_n/\Gamma_f = 1\times10^6$ (Γ_n, decay width for neutron evaporation; Γ_f, fission decay width).

It follows from the considerations above that the mea-

sured nondirect cross section σ_{ND} is not influenced by fusion reaction processes. The decay of a dinuclear complex turns out to be the only possible mechanism to produce the observed cross section at small c.m. angles in the transfer angular distributions.

C. Summary

We have investigated multiproton-transfer reactions in medium heavy systems at three energies below, at, and above the barrier. Mass integrated Q-value spectra and mass and excitation energy integrated angular distributions for transfers of up to four protons have been measured. From the Q-value spectra it can be concluded that the reaction products are predominantly weakly excited, i.e., a cold transfer process had occurred. This observation is supported by the transfer probabilities — they are deduced from the angular distributions — showing that the pairing of the protons is preserved, even after the transfer of four protons.

The measured angular distributions for the one-proton transfer and partially two-proton transfer agree with predictions of DWBA calculations, whereas the three- and four-proton transfers show distinct deviations in the forward angular region. The origin of the enhanced cross sections in this angular region is attributed to nondirect reaction processes, namely, the decay of a long-lived dinuclear complex. The formation of a dinuclear complex in the present systems is probably supported by stabilizing shell effects, predicted for the mass region and octupole deformations corresponding to the measured exit channels.

Applying a simple dynamical model for these processes, lifetimes of the cold dinuclear complexes were determined. The resulting lifetimes are only about twice the collision time.

[1] G. Wolschin, in Approaching Equilibrium in Heavy-Ion Collisions, Proceedings of the International School of Physics "Enrico Fermi," Course LXXVII, Varenna, 1979, edited by R.A. Broglia and R.A. Ricci (North-Holland, Amsterdam, 1981), p. 508.

[2] A. Gobbi, Nucl. Phys. **A354**, 337c (1981).

[3] J.R. Huizenga, in *Deep Inelastic and Fusion Reactions with Heavy Ions*, edited by W. von Oertzen, Lecture Notes in Physics Vol 117 (Springer, Berlin, 1980), p. 1.

[4] R. Künkel, W. von Oertzen, B. Gebauer, H.G. Bohlen, H.A. Bösser, B. Kohlmeyer, F. Pühlhofer, and D. Schüll, Z. Phys. A **336**, 71 (1990).

[5] D. Cline, Nucl. Phys. **A520**, 493c (1990).

[6] K.E. Rehm, C. Beck, A. van den Berg, D.G. Kovar, L.L. Lee, W.C. Ma, F. Videbæk, and T.F. Wang, Phys. Rev. C **42**, 2497 (1990).

[7] J. Speer, W. von Oertzen, D. Schüll, M. Wilpert, H.G. Bohlen, B. Gebauer, B. Kohlmeyer, and F. Pühlhofer, Phys. Lett. B **259**, 422 (1991).

[8] H. Esbensen and S. Landowne, Nucl. Phys. **A494**, 473 (1989).

[9] G.R. Satchler, M.A. Nagarajan, J.S. Lilley, and I.J. Thompson, Ann. Phys. **178**, 110 (1987).

[10] N. Rowley, Nucl. Phys. **A538**, 205c (1992).

[11] J. Dudek, T.R. Werner, and Z. Szymanski, Phys. Lett. B **248**, 235 (1990).

[12] S. Åberg, H. Flocard, and W. Nazarewicz, Ann. Rev. Nucl. Part. Sci. **40**, 439 (1990).

[13] H.G. Clerc, W. Lang, M. Mutterer, C. Schmidt, J.P. Theobald, U. Quade, K. Rudolph, P. Ambruster, F. Gönnenwein, H. Schrader, and D. Engelhardt, Nucl. Phys. **A452**, 277 (1986).

[14] M. Wilpert, B. Gebauer, W. von Oertzen, Th. Wilpert, E. Stiliaris, and H.G. Bohlen, Phys Rev. C **44**, 1081 (1991).

[15] B. Gebauer, H. Lettau, and H. Siekmann, Wiss. Ergebnisbericht, Report No. HMI-294, 1978 (ISSN 0440-0836), p. 49; B. Gebauer, D. Fink, P. Goppelt, M. Wilpert, and Th. Wilpert, Nucl. Instrum. Methods Phys. Res. Sect. B **50**, 159 (1990).

[16] B. Gebauer and Th. Wilpert, Wiss. Ergebnisbericht Report No. HMI-B-420, 1984 (ISSN 0175-8349), p. 94; Th. Wilpert, Diplomarbeit, Hahn-Meitner-Institut, 1985 (unpublished).

[17] U.L. Businaro and S. Gallone, Nuovo Cimento **1**, 1277 (1955).

[18] W. Nörenberg, in *Heavy Ion Collisions*, edited by R. Bock (North-Holland, Amsterdam, 1980), Vol. 2, p. 1.

[19] V.E. Viola, Jr., Nucl. Data **A1**, 391 (1966).

[20] V.E. Viola, K. Kwiatkowski, and M. Walker, Phys. Rev. C **31**,1550 (1985).

[21] W.W. Wilcke, J.R. Birklund, H.J. Wollersheim, A.D. Hoover, J.R. Huizenga, W.U. Schröder, and L.E. Tubbs, At. Data Nucl. Data Tables **25**, 389 (1980).

[22] W. von Oertzen, H.G. Bohlen, B. Gebauer, R. Künkel, F. Pühlhofer, and D. Schüll, Z. Phys. A **326**, 463 (1987).

[23] R. Vandenbosch and J.R. Huizenga, *Nuclear Fission* (Academic, New York, 1973).

[24] S. Cohen, F. Plasil, and W.J. Swiatecki, Ann. Phys. **82**, 557 (1974).

[25] W. Reisdorf, J. Phys. G **20**, 1297 (1994), p. 1315ff.